An Experimental Study of the Aerodynamics and Performance of a Vertical Axis Wind Turbine in a Confined and Unconfined Environment

Vincenzo Dossena[1]
Dipartimento di Energia,
Laboratorio di Fluidodinamica delle Macchine,
Politecnico di Milano,
Via Lambruschini 4,
Milano I-20156, Italy
e-mail: vincenzo.dossena@polimi.it

Giacomo Persico
Dipartimento di Energia,
Laboratorio di Fluidodinamica delle Macchine,
Politecnico di Milano,
Via Lambruschini 4,
Milano I-20156, Italy

Berardo Paradiso
Dipartimento di Energia,
Laboratorio di Fluidodinamica delle Macchine,
Politecnico di Milano, Via Lambruschini 4,
Milano I-20156, Italy

Lorenzo Battisti
Department of Civil, Environmental
and Mechanical Engineering,
Università degli Studi di Trento,
Interdisciplinary Laboratory
of Energetic Technologies,
Via Mesiano 77,
Trento I-38123, Italy
e-mail: lorenzo.battisti@unitn.it

Sergio Dell'Anna
Department of Civil, Environmental
and Mechanical Engineering,
Università degli Studi di Trento,
Interdisciplinary Laboratory
of Energetic Technologies,
Via Mesiano 77,
Trento I-38123, Italy

Alessandra Brighenti
Department of Civil, Environmental
and Mechanical Engineering,
Università degli Studi di Trento,
Interdisciplinary Laboratory
of Energetic Technologies,
Via Mesiano 77,
Trento I-38123, Italy

Enrico Benini
Department of Civil, Environmental
and Mechanical Engineering,
Università degli Studi di Trento,
Interdisciplinary Laboratory
of Energetic Technologies,
Via Mesiano 77,
Trento I-38123, Italy

[1]Corresponding author.

Manuscript received February 16, 2015; final manuscript received April 21, 2015;
published online May 14, 2015.

Introduction

Based on a completely different working principle with respect to the widespread horizontal axis wind turbine, the VAWT is characterized by inherently unsteady aerodynamics, resulting in a highly distorted and time-dependent wake downstream of the machine. The existence of different VAWT architectures (troposkian blade, H-blades, V-Blades, and Gorlov type-blades) further complicates the formulation of general design guidelines for this class of machines. These difficulties have historically prevented the system-atic optimization of VAWTs [1,2], thus limiting the widespread use of this technology on a large market scale; however, the VAWT architecture exhibits a number of advantages such as: insensitivity to yaw, ability to withstand rapid changes of wind direction, and low noise emissions due to low tip-speed ratios. In this scenario, experimental investigations on VAWT are crucial to provide new insights on the turbine flow physics, to achieve reli-able estimates of the turbine performance, and to support the vali-dation of numerical models [2].

In recent years, the renewed interest on community VAWTs (i.e., small-scale turbines [3]) has produced several academic and industrial projects in which novel configurations, or revisited established solutions, are investigated from the performance and structural point of views. Community VAWTs offer, due to model sizes and operating envelope, the possibility of real-scale testing in wind tunnels. In the wind turbine development phase, R&D costs are remarkably reduced, and many safety issues and basic operating procedures (control system, brake, start-up, shutdown, etc.) can be tested. On the other side, limits of such tests are the near zero turbulence level experienced by the turbine, the steady-state environmental conditions, and the tunnel wall interference.

Although controlled and repeatable, wind tunnel testing is affected by the difficulty in evaluating the blockage effects on the turbine performance. As the wind turbine is an extended turbomachine, the stream-tube forming past it deforms dynamically as the wind condition and the wind turbine settings change. Additionally, the wind turbine is a rotating body and considering in particular the VAWT architecture, the resulting wake can be deflected crosswise downstream [4] and depends on the rotor tip-speed ratio [4,5]. Furthermore, due to the inherent unsteadiness of VAWT aerodynamics, the far and near wake are highly time-dependent, even for stationary upwind inflow conditions. These features exhibit a complex combination with the wind tunnel flow and, consequently, a variable wall interference establishes during wind tunnel tests. Experiments in open test-section (unconfined environment) alleviate these problems, because the flow can expand around the objects and in a certain sense resemble the conditions expected in an open environment; however, specific correlations are often applied to predict the wind turbine behavior in open field.

An experimental research program on VAWTs was carried out by the authors in the frame of an Italian National founded project ("PRIN 2009—Fluid dynamic analysis of vertical axis wind turbines," 2011–2013). Two wind turbines (troposkian-blade and H-blade) operating in several flow conditions were considered in the project, with the aim to give insights into the different aerodynamics of the investigated architectures and to compare the results with that of similar projects. This paper presents part of the results obtained for the H-type turbine, as an extension of a preliminary research previously performed on the same turbine configuration [4]. The turbine was tested in real-scale setup, thus satisfying the full dynamic similitude in terms of tip-speed ratio and Reynolds number. Integral turbine torque and power measurements were obtained by dedicated onboard instrumentation. Detailed aerodynamic measurements were performed with conventional five-hole probes and miniaturized hot wires for time-resolved velocity measurements. The local unsteady flow field resolved in phase with the rotor position was derived by hot wire measurements performed for the near and far field downstream of the turbine. The streamwise turbulent velocity component was also extracted and analyzed.

By applying the present technique, clear pictures of the 3D turbine wake can be achieved; in the few works available in literature about flow measurements in VAWT [6–10], PIV is used to obtain a similar flow representation and to investigate the vortex generation and shedding during the blade revolution. As an alternative way, computational fluid dynamics can be used to investigate the turbine wake and blockage effects for a VAWT in wind tunnel, but further investigations may be needed [11,12].

In the present research, also the wake–tunnel interaction and the tunnel blockage effects are considered. As a matter of fact, no correlations are available for wind tunnel blockage correction specifically developed for VAWT, and in general a substantial lack of methods is found for rotating objects with variable volume wakes. Among them, the early works of Glauert [13,14] and more recently the model proposed by Mikkelsen and Sørensen [15,16] have been considered for comparison purpose in the present research.

The paper is structured as follows. At first, the experimental techniques and the tested model are briefly described, and then an analysis of the turbine performance is presented alongside a quantitative discussion of the blockage effect and its correction. The time averaged and time-resolved flow field are finally presented for two different traverses downstream of the turbine in three different operating conditions.

Experimental Methodology

The present paper provides a comprehensive experimental study performed on a VAWT in a wind tunnel environment, car-ried out by applying several measurement techniques including mechanical, structural, and aerodynamic devices. In this way, both the integral performance of the machine and the detailed flow field upstream and downstream of the model are experimen-tally determined. In the following, a review of the experimental setup, of the turbine model, and of the test plan is reported.

Wind Tunnel. Experiments were performed in the Politecnico di Milano large-scale wind tunnel, which consists in a closed loop facility developing along two floors of a dedicated building. Within the facility, two different test sections are available: a low-speed test section (14 m width $\times$ 3.84 m height) allowing a maxi-mum air velocity of about 15 m/s, and a high-speed section (4 m $\times$ 3.84 m) allowing a maximum velocity of 55 m/s. The wind generator is composed by two rows of seven fans, each of them driven by an inverter controlled electric motor. The overall installed electric power is approximately 1.4 MW.

Tests were performed in the high-speed test section, located immediately upstream of the diffuser leading to the fans, and characterized by a very low turbulence level ($<1\%$).

Tests can be carried out in confined environment, here defined as Closed Chamber (CC) configuration, by positioning the models inside of a removable test room of 4 m width and 3.84 m height; as an alternative, unconfined or Open Chamber (OC) configura-tion can be achieved by removing the test room and installing the models directly facing the upstream tunnel tube. The same VAWT was tested in both the CC and OC configurations in order to analyze the influence of the model blockage for different oper-ating conditions.

Figure 1(a) reports a sketch of the experimental setup in the OC configuration, alongside the locations of the aerodynamic measurement planes; a dashed line is also provided to show the CC trace when operating in confined environment. A picture of the turbine and of the probe traversing system in CC is reported in Figure 1(b). The model was centered in both configurations. A solid blockage ratio $\sigma = 0.10$ results in the closed room, where the frontal section of the model is given by $A_D = 2H \times D$.

VAWT Model. The tested real-scale VAWT is a three bladed H-shaped Darrieus; blades are made with a wood core and a car-bon fiber reinforced polymer (CFRP) shell. Two aluminum spokes joint blades to the support steel pole, as shown in Fig. 2. The rotor has swept area of 1.5 m^2 ($2H \times D$, 1.5 m $\times$ 1.028 m), and it is equipped with dihedral blades composed by unstaggered NACA0021 profiles ($c = 0.086$ m). The rotor prototype was designed by the Company Tozzi-Nord Wind Turbines, while the test stand and the data acquisition system were designed by the staff of University of Trento.

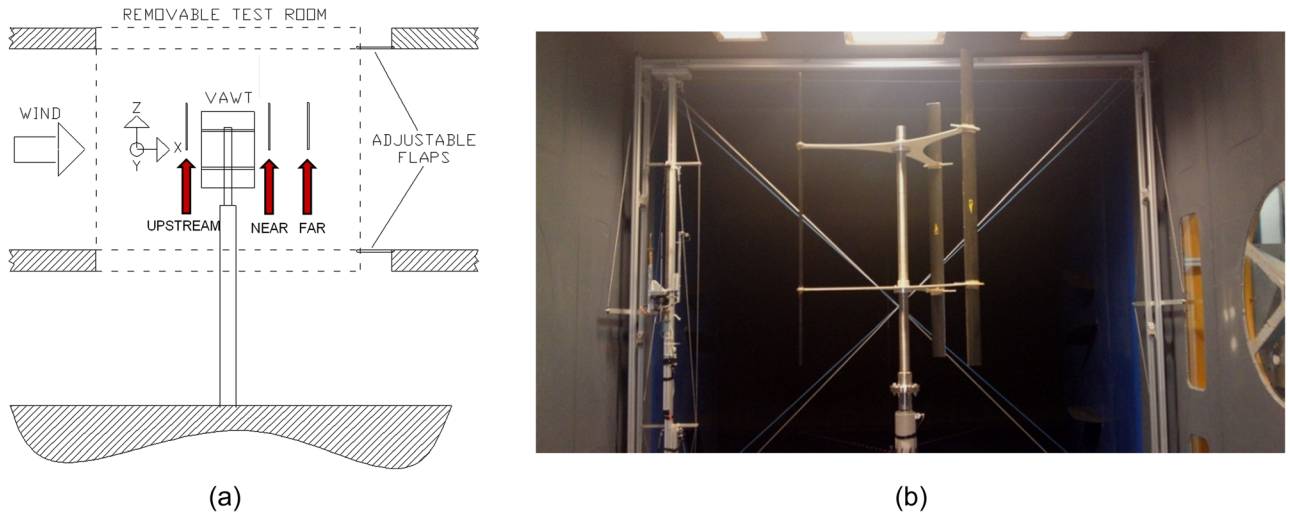

Fig. 1 (*a*) Sketch of measurement section and (*b*) picture of the VAWT and the traversing system in CC configuration

Mechanical Measurement Techniques. The H-shaped Darrieus rotor (blades and tower, Fig. 2(*a*)) was connected to the power and measurement train as shown in Fig. 2(*b*), and the turbine performance was measured by applying:

- two *axial accelerometers* mounted in the upper part of the supporting mast to monitor the streamwise and longitudinal vibrations of the structure;
- two whole *strain gauge bridges* installed on the rotor mast in order to measure streamwise and longitudinal aerodynamic thrusts;
- an *absolute encoder* to provide the rotational speed and the rotor phase (azimuthal position of the reference blade);
- a *precision torque meter* mounted between elastic joints to measure the torque transmitted through the shaft.

Data were acquired by a Compact-RIO (National Instruments, Austin, TX) device, setting a sampling frequency of 2 kHz. Recorded time series lasted 3 min for each working condition, in order to guarantee a sufficient amount of data for ensemble averaging on the rotor azimuthal position. The reversible electrical machine mounted on the power train (see Fig. 2(*b*)) was con-trolled by an inverter to guarantee constant rotational speed during the tests.

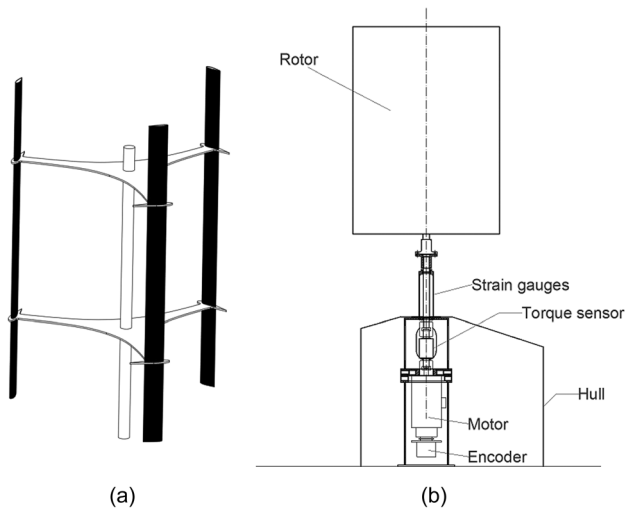

Fig. 2 (*a*) H-shaped Darrieus rotor tested in wind tunnel and (*b*) sketch of the power train

The data reduction process was performed by combining several operations, according to the procedure described below:

- each measurement time series is first divided into 20 s bins in order to compute the mean values, i.e., 3 min record is divided in six bins represented by their mean values; in this way, standard deviation of each bin contains information about possible unsteadiness in the machine operation;
- the power and thrust curves are then computed starting from the bin averaged values;
- the standard deviation of the measurements is computed over the averaged bin values and then the measurement error (Type A) is determined according to the standard proposed in Ref. [17] for a confidence interval of 95% (standard deviation is hence computed between the bin averaged values);
- the sensor uncertainties (Type B) are taken by the datasheet of the sensor manufacturers;
- the reference wind speed value and its uncertainty were provided by the wind tunnel manager before each test;
- the derived measurement error propagation is computed following the guidelines provided in Ref. [17].

Aerodynamic Measurement Techniques. To determine the flow field upstream and downstream of the model, both aerodynamic pressure probes and hot wire anemometers were traversed on several measurement planes.

In particular, a *directional pneumatic five hole probe* was applied to detect the total and static pressure and the 3D velocity vector. The probe was calibrated on a low-speed jet over an angular range of ± 24 deg in both the flow angles, here defined as: the yaw angle, measured on the XY plane, i.e., the one normal to the turbine axis; the pitch angle, measured on the XZ plane, i.e., the one between the axial and the streamwise directions. Uncertainty in total and static pressure measurements resulted within 10 Pa, while the uncertainty on the flow angle measurements was evaluated as ± 0.2 deg.

To measure the time-resolved velocity field, two *single-sensor hot wire anemometers* were applied. The sensor wires, mounted normal to the probe stem, have a diameter of 5 μm and are operated in constant temperature mode. Uncertainty in the velocity measurements resulted about 2% after calibration in a low-speed jet. The first hot wire probe was mounted in streamwise (X) direction, so to minimize the wire sensitivity to the flow angles (which anyhow are expected to be small in this application). Hence, no specific directional calibration is required and the output of this first probe is the velocity magnitude. The second probe was mounted in axial (Z) direction, so the wire was exposed to the flow in transversal (Y) direction. Mounted in this way, the probe is

sensitive to both the streamwise and transversal velocity components; to determine the velocity components and thus the yaw angle a dedicated angular calibration was performed and the probe was rotated around its axis in three angular positions, namely, +45 deg, 0 deg, and −45 deg with respect to the transversal direction (one in excess to improve the accuracy in the reconstruction).

Hot wire data allowed to define, for each point of the measurement grid, the time averaged and the time-periodic fluctuation of the flow velocity, as a function of the rotor angular position. The time-periodic component was obtained by ensemble averaging, using the encoder mounted on the rotor as key-phasor. The turbulence intensity was also determined, by extracting the unresolved unsteady component from the hot wire data.

Test Plan. To determine the performance curve of the turbine, several operating conditions were simulated. The fairly large range of conditions investigated in the current tests was obtained by keeping constant the rotational speed of the rotor at 400 rpm, and by modifying the wind speed ranging from 6 to 16 m/s. The maximum rotational speed was limited to avoid structural problems of the turbine rotor, while the minimum wind speed was limited by the measurement accuracy. The wind tunnel was set at a given operating condition, and, once stable flow configuration was established, experimental data were taken. The tunnel wind speed was then increased, with steps of about 1 m/s, to the next operating point. At every 3–4 operating points, the wind tunnel flow and the rotor were stopped in order to acquire the sensor offsets.

Aerodynamic measurements were performed on three different planes (as previously shown in Fig. 1(*a*)) normal to the stream-wise direction, located, respectively, 1.5 *D* downstream of the VAWT (called *far*), 0.75 *D* downstream of the VAWT (called *near*), and 0.75 *D* upstream of the VAWT (called *upstream*). Thanks to the symmetry with respect to midspan, the planes cover the upper half of the rotor and exceed the tip of the blades by 25%of the half-blade span, so to investigate the wake enlargement also in spanwise direction. The measurement grids in transversal (*Y*) direction also largely exceed the machine dimension (∼3 times the rotor diameter), so to properly capture the wake enlargement downstream of the rotor. The flow on these planes was investigated for three wind speeds, corresponding to three relevant values of tip-speed ratio (λ):

- $\lambda \cong 3.5$ (high-load condition)
- $\lambda \cong 2.5$ (maximum C_P condition)
- $\lambda \cong 1.5$ (low-load condition)

The $\lambda = 1.5$ condition is in the ascending branch of the C_P–λ curve, where the blades are expected to stall for a significant portion of the rotor revolution, while for $\lambda = 2.5$ the rotor works near the maximum C_P condition.

Turbine Performance and Blockage Effect

In this section, the overall turbine performance is discussed in detail, on the basis of thrust and power measurement data; a comparison between the confined and the unconfined configurations is also proposed to quantify the impact of blockage.

Turbine Performance in Unconfined Environment. Figures 3 and 4 show the curves of streamwise thrust and power coeffi-cients versus the tip-speed ratio λ for the OC configuration, also including the measurement uncertainty. The power coefficient curve is limited to $\lambda = 4.5$ because above this limit the power becomes negative. Three sets of data are provided in each figure, corresponding to the three different positions of the traversing system for aerodynamic measurements. The trends show that the position of the traversing system does not influence the turbine performance measurements. The uncertainty tends to reduce as the wind speed increases (and the λ decreases).

The maximum of thrust coefficient occurs at ∼7–8 m/s, while the maximum power coefficient is achieved at ∼8–9 m/s, corresponding to $\lambda \cong 2.5$: in this condition, the power coefficient results 0.28. For lower velocities (or higher λ), a relatively steep reduction of power coefficient occurs, while for higher velocities (or lower λ) the reduction is more gradual.

Influence of Blockage in Unconfined Environment. As solid walls are removed from the test section, an open-jet flow is generated; a certain degree of blockage might, however, remain, preventing the direct extension of open-jet results to the actual open-field operation. Following the analysis proposed in Ref. [18], the open-jet blockage results from several sources: air stream perturbation into the nozzle, perturbation into the jet expansion region, lateral jet deflection, and perturbation into the collector placed downstream the tested model.

Even though the blockage estimation in open-jet configuration was investigated for bluff body flows only [18], a quantitative estimate of this effect is proposed here for the present rotating body. Nozzle blockage effect is evaluated with a simple potential-flow model, which consists of a point source exposed to a parallel flow with stagnation point placed as close as possible to the stagnation point of the real model [18]. In this way, the half-infinite body represents the test body plus its mirror image; however, in the present case, the mirrored body is not used because the rotor is placed just in the wind tunnel center. According to this adaptation of the model, the overall open-jet blockage correction coefficient can be evaluated as

$$\frac{V_0'}{V_0} = 1 + \epsilon_S + \epsilon_N + \epsilon_C \tag{1}$$

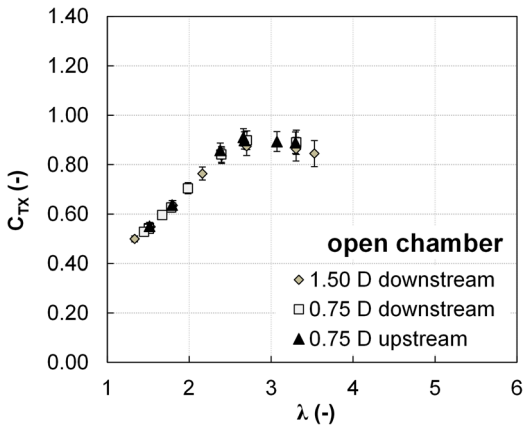

Fig. 3 Streamwise thrust curve coefficient in OC

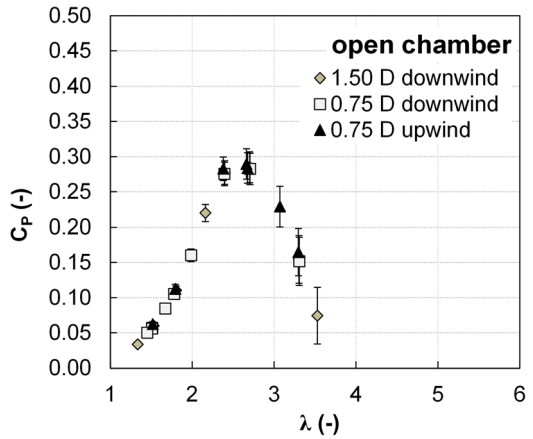

Fig. 4 Power coefficient curve in OC

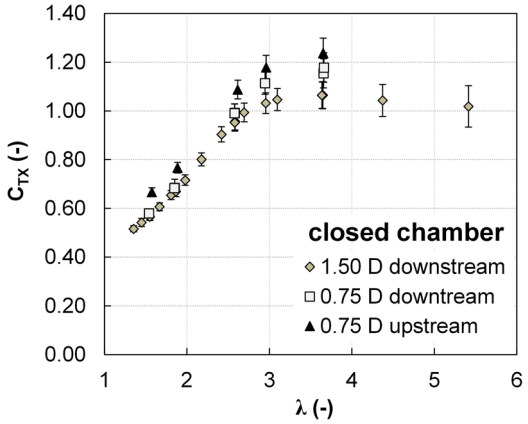

Fig. 5 Streamwise thrust coefficient measured in CC

in which ϵ_S is the induced velocity due to jet expansion, ϵ_N is the induced velocity at model position due to nozzle effect, and ϵ_C is the induced velocity at the model position due to collector effect. The induced velocity ratio V_0'/V_0 allows to determine the open-field wind speed (V_0') that would induce on the turbine the same flow configuration established in the open-jet configuration for a specific wind speed (V_0).

For the present wind tunnel setup, the nondimensional parameters appearing in Eq. (1) can be evaluated by resorting to the expressions proposed in Ref. [18] and result $\epsilon_S = -0.0016$, $\epsilon_N = 0.0034$, and $\epsilon_C = 0.0135$, yielding an overall blockage correction coefficient of $V_0'/V_0 = 1.015$. The negative induced velocity estimated for the jet expansion term (ϵ_S) implies that a lower upstream wind speed would be required to recover the open-field configuration; the opposite stands out for the other two effects, whose coefficients are both estimated as positive. Eventually, the overall open-jet blockage factor is positive and amounts to 1.5%; since, as discussed later, the blockage factor evaluated experimentally in CC configuration is about one order of magnitude larger than the open-jet one, no correction was applied to OC measurements.

Turbine Performance in Confined Environment. Figures 5 and 6 show the streamwise thrust and power coefficients measured in CC configuration. By comparing these curves to their OC counterparts, a very significant blockage effect appears, as the maximum C_{TX} in confined environment rises up to 1.1 from 0.9 in unconfined condition and the maximum C_P exceeds 0.35 in confined environment while remaining below 0.3 in unconfined condition. This indicates that for 10% solid blockage, proper correction methods have to be considered to achieve reliable estimates of VAWT performance in wind tunnel tests.

The increase of force and power exchanged by the machine can be easily explained by considering that the confinement imposed by the tunnel walls accelerates the flow in the turbine region. The impact of blockage is further highlighted by the change in turbine performance observed when the traversing systems are moved. As well visible in Figs. 5 and 6, when the traversing system is installed relatively close to the turbine (upstream and near down-stream traverses are at 0.25 D from the closest blade), it introdu-ces a non-negligible disturbance on the turbine aerodynamic behavior. Apparently, the traversing system introduces a further speed-up across the rotor, resulting in an additional blockage effect that also contributes to enhance the force and power exchanged. For this reason, only mechanical measurement data performed for the traversing system in the far downwind plane are considered for the blockage quantification discussed in the following.

Influence of Blockage in Confined Environment. Once experimental thrust data are available for CC and OC configuration, the experimental blockage coefficient can be determined. Following Glauert [13], the blockage can be expressed in the form of an overspeed in the upstream wind that in OC yields the same thrust measured in CC for a specified wind speed. The upstream overspeed in OC compensates the overspeed induced by the walls in the CC environment, so that the same flow configuration is established on the turbine between CC and OC conditions.

To determine the overspeed ratio, the thrust curves in OC and CC configurations were first analytically interpolated with a sixth degree polynomial, as shown in Fig. 7 (quadratic error $R^2 \cong 0.9998$). The experimental blockage correction coefficient was then computed according to the following procedure:

- a number of wind speed V_{CC} was preliminarily selected and the corresponding CC thrusts were evaluated;
- by inverting the V–T_X relation for OC, the equivalent wind speeds V_{OC} that yields the same CC thrusts previously selected was determined;
- the ratio between the computed V_{OC} and the selected V_{CC} yields the experimental blockage correction coefficient as a function of the upstream wind speed, shown as error bars in Fig. 8.

Figure 8 indicates that the blockage factor of the VAWT increases as the tip-speed ratio λ rises (or as the velocity of the wind reduces). This indicates that, as the rotor speed increases relatively to the wind speed, the machine becomes more "solid"; as a result, the amount of flow that is ingested within the virtual cylinder traced by the blade motion reduces, and a larger amount of

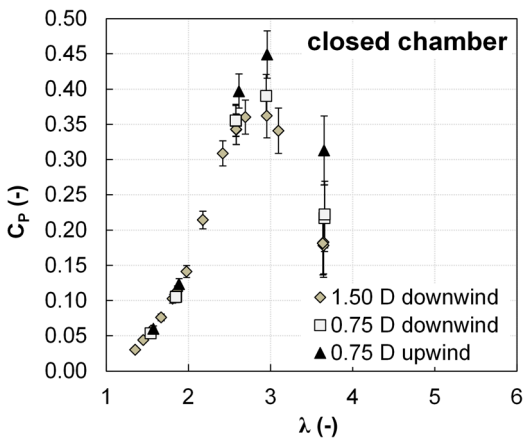

Fig. 6 Power coefficient measured in CC

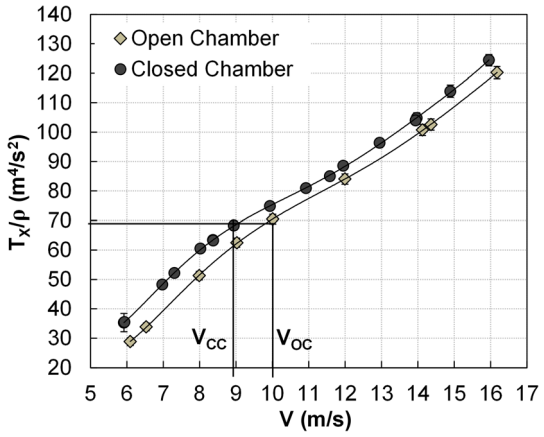

Fig. 7 Experimental thrusts measured in open and closed chamber with their interpolating curves

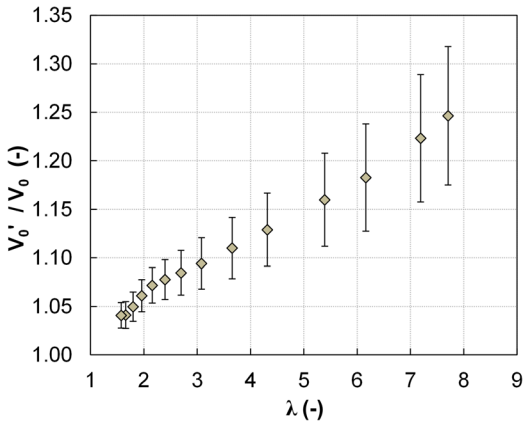

Fig. 8 Experimental blockage correction coefficient V_0'/V_0 versus tip-speed ratio λ

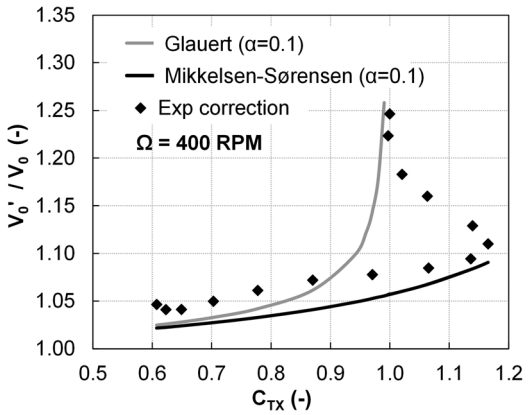

Fig. 9 Blockage correction coefficient V_0'/V_0 versus CC thrust coefficient C_{TX}

flow is forced to move around the turbine. Experimental data show that even at very low λ, for that the blockage effect is mini-mal, the blockage correction coefficient is greater than 1.04.

Since the experimental blockage correction coefficient was found to be quantitatively significant in this configuration, a comparison was carried out against two of the most classical correction models available in literature for wind tunnel testing.

Figure 9 shows the streamwise thrust coefficient versus the experimental blockage correction compared with the blockage models of Glauert [13,14], see Eqs. (2) and (3), and with the model of Mikkelsen–Sørensen [15,16], see Eqs. (4)–(6). According to Glauert, the blockage correction coefficient can be computed as

$$\frac{V_0'}{V_0} = 1 + \alpha \frac{C_{TX}}{\sqrt{1 - C_{TX}}} \tag{2}$$

in which α is the turbine solid blockage, defined as

$$\alpha = \frac{A_D}{A_T} \tag{3}$$

The Mikkelsen–Sørensen velocity correction model reads

$$\frac{V_0'}{V_0} = \beta + \frac{1}{4}\frac{C_{TX}}{\beta} \tag{4}$$

in which the coefficient β is defined as

$$\beta = -\frac{\alpha}{2\alpha - 1}\frac{\alpha^2\sigma - 1}{\sigma\alpha(3\alpha - 2) + 1} = -\frac{\alpha}{2\alpha - 1}F(\sigma, \alpha) \tag{5}$$

and the coefficients σ and α are the blockage of the downstream wake ($A_{w,d}$) and the solid blockage, respectively, defined as

$$\sigma = \frac{A_{w,d}}{A_D} \quad \alpha = \frac{A_D}{A_T} \tag{6}$$

Since the function $F(\sigma, \alpha)$ is always greater than one, the disk velocity in confined environment is higher than that established in unconfined environment. As visible in the above expressions, the Glauert model only resorts to the solid blockage and thrust coefficients, while the Mikkelsen–Sorensen model also requires information on the wake area ($A_{w,d}$) downstream of the turbine.

The trends reported in Fig. 9 show that both the models correctly predict the increase of blockage at higher thrust, but they tend to underpredict the experimental blockage correction (the unique exception being the Glauert model which has a singularity as C_{TX} approaches 1); the Mikkelsen–Sørensen model seems to better capture the trend below $C_{TX} = 1$, but it significantly underestimates the experimental values. Moreover, the Mikkelsen–Sørensen model does not capture the steep increase of blockage observed in the experiments for very low wind speed (lower than 5.9 m/s), visible from the sharp hook found for $C_{TX} > 1$.

Considering two operating conditions in particular, whose details are provided in Table 1, the Mikkelsen–Sørensen model predicts wake areas of $\sim$2.06 m^2 at 5.9 m/s ($\lambda \cong 3.5$) and of $\sim$1.83 m^2 at 13.7 m/s ($\lambda \cong 1.5$); experimental data reported in the following (see Figs. 11 and 14) indicate wake areas of $\sim$2.4 m^2 and $\sim$1.26 m^2 for 5.9 m/s and 13.7 m/s, respectively (assuming that the wake starts when the wind deficit exceeds 10%). It is apparent that the Mikkelsen–Sørensen model also fails in estimat-ing the disturbed area. This leads to infer that the theoretical blockage models for VAWT need improvement, especially to introduce a realistic evolution of the wake inside the tunnel. In the following, the time-mean and time-resolved wake shed by the VAWT is discussed.

Time-Mean Analysis of VAWT Wake

In this section, the characteristics of the wake measured downstream of the turbine are presented and discussed for the three operating conditions recalled in the "Experimental Methodology" section, namely, for $\lambda \cong 1.5$, 2.5, and 3.5. Hot wire anemometer data were processed to determine the velocity magnitude and the yaw angle; the velocity was then made nondimensional using the upstream wind speed.

Prior to analyze the flow downstream of the turbine, a recall of the machine operation is provided by referring to the schematic depicted in Fig. 10. During a full revolution, the interaction of one blade with the wind can be roughly divided in a "downwind" phase ($0 < Y/D < 0.5$), and in an "upwind" one ($-0.5 < Y/D < 0$); the blade works with different ranges of angles of attack in the

Table 1 Comparison between experiments and prediction with Mikkelsen–Sørensen [15,16] blockage model

V_{CC} (m/s)	Λ	$C_{TX,exp}$	$A_{3,exp}$ (m^2)	$(V'_0/V_0)_{exp}$	$A_{3,M\text{-}S}$ (m^2)	$(V'_0/V_0)_{M\text{-}S}$
5.9	3.5	1.165	2.4	1.110	2.065	1.091
13.7	1.5	0.623	1.26	1.041	1.83	1.028

two phases, the downwind phase being the most critical for the aerodynamics of the profiles.

Figure 11 reports the distributions of flow velocity magnitude downstream of the turbine for different measurement traverses and operating conditions in OC configuration; a rectangular line is also added to trace the turbine cross section. The velocity field clearly shows the trace of the wake, which strongly changes its shape and extension as the tip-speed ratio is altered. In particular for the highest λ (Fig. 11(a)), the wake extends well beyond the turbine cross section and further enlarges passing from near to far traverses. In the same operating regime, the wake has a nearly symmetrical shape up to ~60% of the half-blade span, with almost null velocity in a wide region around the turbine axis. In the blade tip region, a complex wake border is observed, with two regions of velocity defect on the turbine sides.

As the tip-speed ratio is reduced, the aerodynamic loading reduces as well and for the lowest λ (Fig. 11(c)) the extension of the wake region approaches the dimension of the model cross section; at low loading the wake loses its symmetrical shape at mid-span, as a larger velocity defect is found all along the span in the region $-0.5 < Y/D < 0.0$. This feature amplifies as the wake develops downstream, resulting in an inclined tip border at the far traverse position. The yaw angle distribution, reported in Fig. 12 for $\lambda = 1.5$, adds further elements to the severe asymmetry in the flow configuration. In particular, in the region $-0.5 < Y/D < 0.0$, a large-scale structure is observed across the tip of the blade, characterized by high spanwise gradient in yaw angle. This structure is consistent with the time-mean trace of the tip vortex and disappears on the right side of the turbine.

The asymmetry in the wake and tip vortex depends on the time-dependent aerodynamics of the blades as they undergo a full rotor revolution. As depicted in Fig. 10, the blades traveling in the region $-0.5 < Y/D < 0.0$ move upwind, namely, "against" the wind speed; in this portion of the revolution, aerodynamic stall is limited or inhibited even at high tip-speed ratio, resulting in a high lift established on the blades; this leads to a more stable flow in the mid region and to the onset of a strong vortex at the blade tip. In the downwind phase of the revolution, dynamic stall nor-mally occurs (especially at medium-low tip-speed ratios, see Ref.[19] for a schematic of the flow configuration in the different phases of the blade revolution in a VAWT); in this condition, very small lift establishes on the blade and, hence, the vortex generated at the tip of the blade results negligible on a time-mean basis. The additional tip losses connected to the vortex on the upwind side of the turbine are responsible for the inclined wake border at the tip.

The double peak in the wake tip border observed for $\lambda = 3.5$ can be explained by considering that, as discussed in the following when considering the wake unsteadiness, dynamic stall is avoided in this condition for most part of the revolution. This reduces the periodic evolution of the blade tip vortex, which now holds for the whole period. However, higher aerodynamic forces are still induced in the upwind phase of the revolution, leading to a stronger tip vortex in the upwind part of the machine; this justifies the

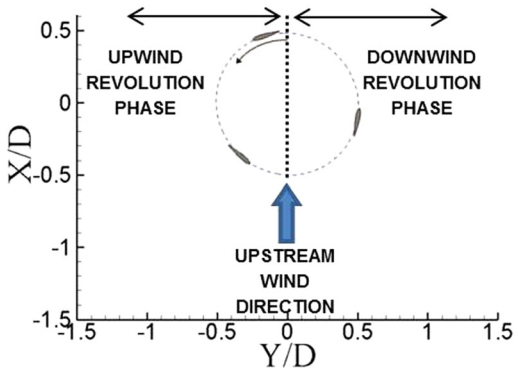

Fig. 10 Schematic of VAWT operation

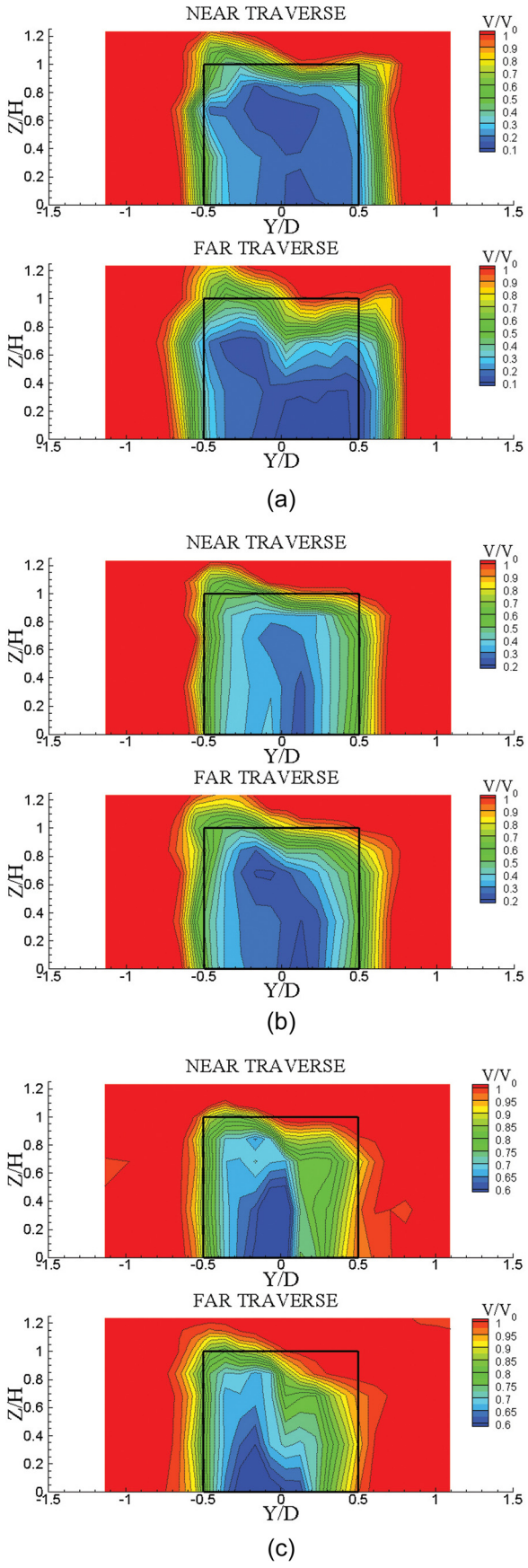

Fig. 11 Turbine wake for different loading conditions in OC configuration: (*a*) high loading case: $\lambda = 3.5$, (*b*) midloading case: $\lambda = 2.5$, and (*c*) low loading case: $\lambda = 1.5$

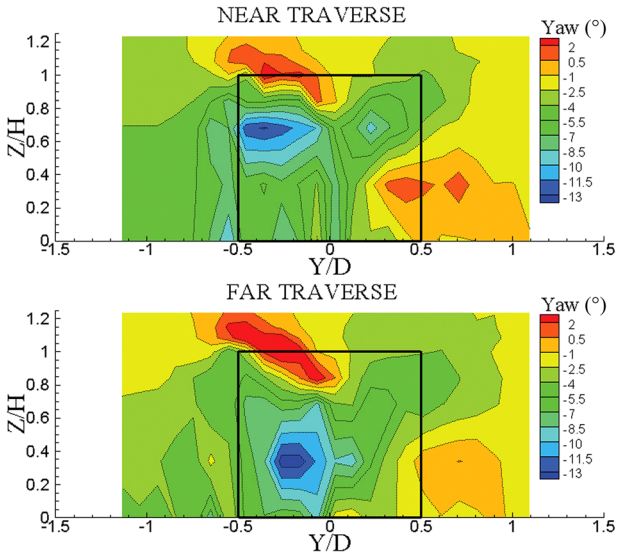

Fig. 12 Flow angle distribution at low loading conditions (λ = 1.5, V_0 = 14.2 m/s) in OC configuration

nonsymmetric wake shape observed at the tip also in this operating conditions.

Figure 13 shows the velocity and flow angle distributions on the near traverse for $\lambda = 1.5$ in CC configuration. As expected, due to the blockage effect an overspeed of the flow with respect to the upstream wind is found outside of the wake. The wake, instead, retains most of the features observed for OC configuration, exhibiting a nonsymmetric shape both at midspan and in the tip vortex region. In fact, the time-mean tip vortex appears slightly stronger than that observed in OC configuration and not extended above the turbine tip section; this is probably due to the higher momentum of the flow outside of the wake with respect to the OC flow field.

Figure 14 shows the comparison between the wake measured for high and low tip-speed ratio at the far traverse in CC configuration. As found for OC, the wake reduces significantly in both velocity defect and extension as the tip-speed ratio reduces. It is interesting to note that the overspeed outside of the wake almost doubles when the λ raises from 1.5 to 3.5; this is consistent with the findings of the blockage analysis: by raising the tip-speed

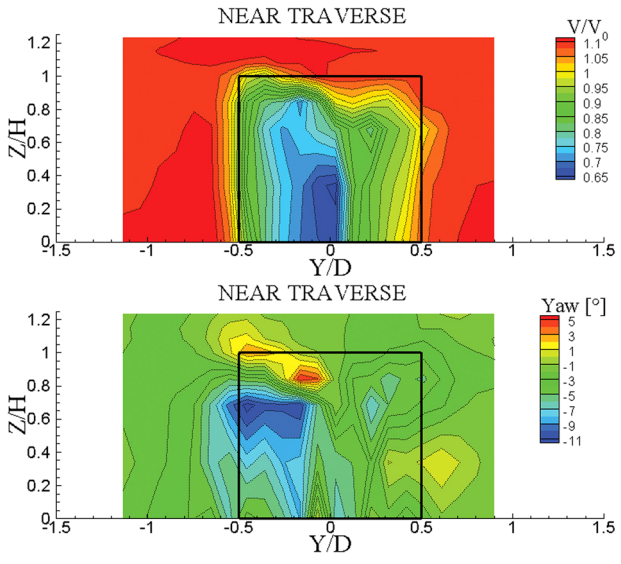

Fig. 13 Turbine wake for low loading ($\lambda = 1.5$, $V_0 = 13.7$ m/s) in CC configuration (near traverse only)

ratio, the blockage factor increases as well, inducing a higher acceleration of the flow in the stream-tube outside the wake.

VAWT Wake Unsteadiness. VAWTs are characterized by an inherent aerodynamic unsteadiness as a result of the periodic evolution of the angle of attack on the profiles. For this reason, blade wakes and tip vortices shed in the stream-tube downstream of the turbine undergo periodic fluctuations phase-locked to the rotor. Depending on the Reynolds number and the operating conditions, the variation of angle of attack on the blades during the revolution can be sufficiently large to exceed the stall limit of the profile, triggering separation for a significant portion of the revolution; in these conditions an even higher unsteadiness is generated in the turbine wake.

Time-resolved velocity measurements performed with hot wire anemometry are now presented to characterize the wake unsteadiness of the VAWT studied in this work. To better highlight the different dynamic components of the velocity field downstream of the turbine, the unsteady velocity signals were first phase-locked on the rotor passage, and then ensemble-averaged using the rotor revolution as fundamental period. The unresolved component of the velocity fluctuation, defined as the difference between the instantaneous signal and its periodic component, was then used to obtain the turbulence intensity for each phase on the revolution period.

Figure 15 reports the phase-resolved velocity magnitude and turbulence intensity for two operating conditions in OC configuration, in the form of two-dimensional space–time diagrams at midspan. These diagrams allow to distinguish the time-dependent structures, appearing as vertical gradients, from the time-averaged ones, characterized by horizontal gradients. Both the near and far downstream traverses are considered, to highlight the effect of the mixing process on the rotor viscous structures.

The distributions reported in Fig. 15 show a significant dependence of the wake unsteadiness on the operating conditions. For high tip-speed ratio (Fig. 15(*a*)), no unsteadiness appears in the velocity field at midspan, as indicated by the negligible vertical gradients observed in both the traverses. The flow is dominated by the transversal gradients found at the edges of the turbine wake,

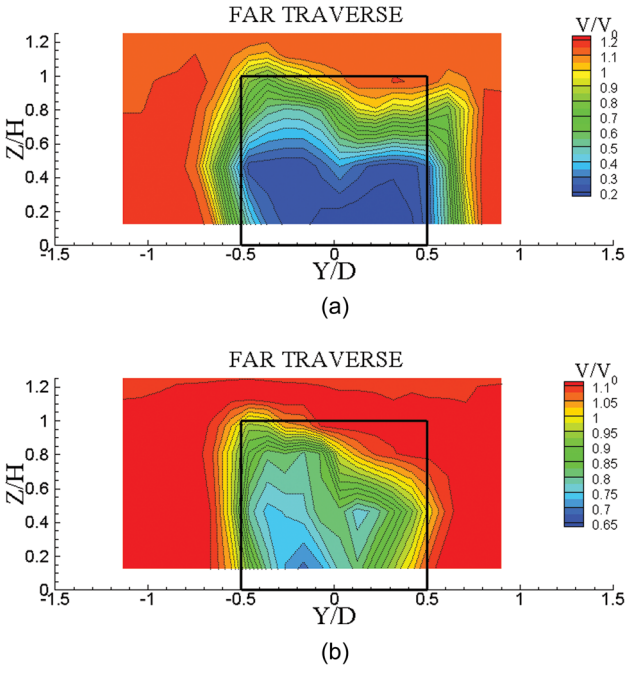

Fig. 14 Turbine wake for different loading conditions in CC configuration (far traverse only): (*a*) high loading case: $\lambda = 3.5$ ($V_0 = 5.9$ m/s) and (*b*) low loading case: $\lambda = 1.5$ ($V_0 = 13.7$ m/s)

which appear as nearly uniform vertical bands just beyond the geometrical limits of the machine (marked in the figure by two black dotted lines). These high-gradient regions are also characterized by a very large turbulence intensity, due to the significant turbulent transport activated in the shear layer generated between the turbine wake and the external flow. In fact, the high turbulence band centered at $Y/D = 0.5$ shows, for the near traverse, traces of blade-periodic phenomena in the form of three peaks of turbulence intensity; on the contrary, no unsteady traces appear on the other side of the wake. This feature can be explained by considering that the right side of the wake results from the interaction between the turbine and the flow in the downwind blade motion, where the largest fluctuations of angle of attack occur; however, the weak periodic traces observed at the near traverse are rapidly mixed-out and disappear in the far measurement position, where an almost steady wake is measured.

The steady velocity field in the turbine wake indicates that the wakes of the profiles are completely mixed-out and also suggests that no relevant dynamic stall phenomena occur at high tip-speed ratio. Time–space plots for maximum power coefficient ($\lambda = 2.5$),

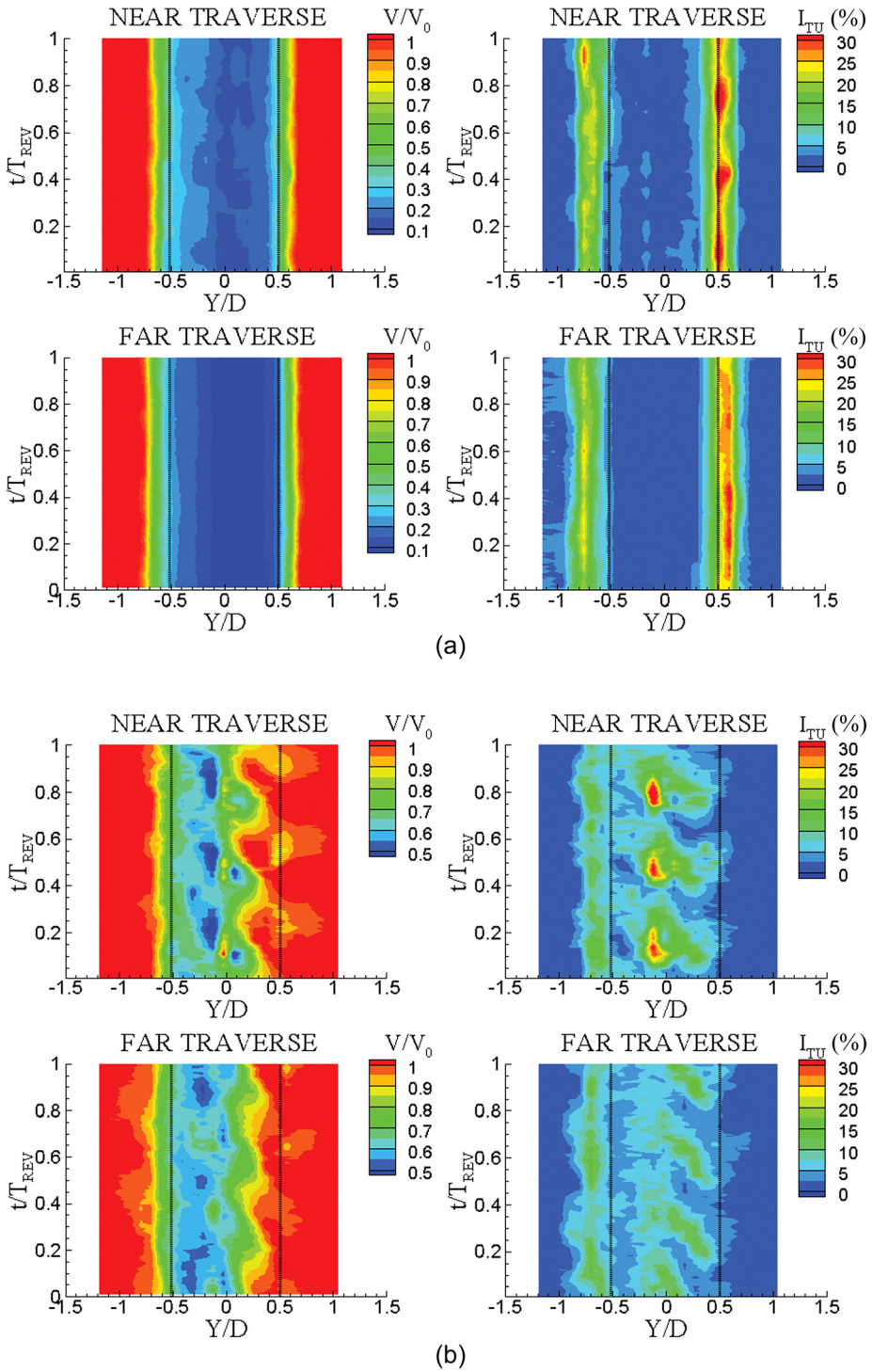

Fig. 15 Space–time wake representation at midspan for different operating conditions in OC configuration: (*a*) high loading case: $\lambda = 3.5$ ($V_0 = 6.5$ m/s) and (*b*) low loading case: $\lambda = 1.5$ ($V_0 = 14.2$ m/s)

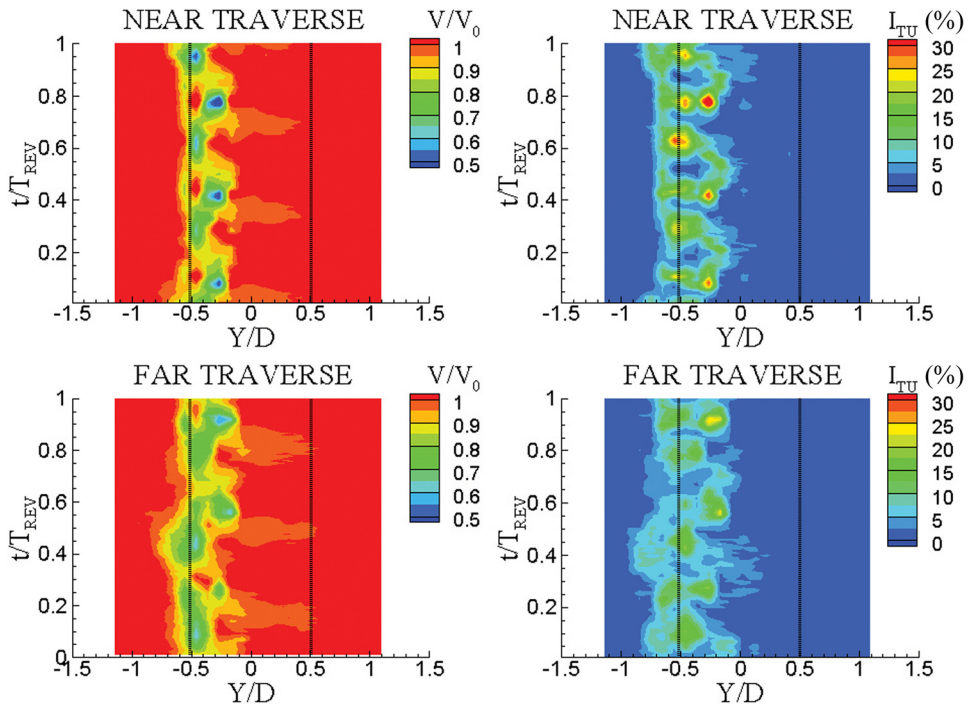

Fig. 16 Space–time wake representation at the turbine tip section for $\lambda = 1.5$ in OC configuration

not reported for sake of brevity, still show a steady wake at midspan. The oscillation in angle of attack is indeed highly dependent on the tip-speed ratio, reducing as the tip-speed ratio increases; further experiments in intermediate operating conditions suggest that, for this machine, large-scale dynamic stall is not relevant for $\lambda > 2.1$.

For the lowest tip-speed ratio, a completely different flow configuration is found. Figure 15(*b*), which provides the velocity and turbulence evolution for $\lambda = 1.5$, shows significant unsteady features on both the traverses. The asymmetry between the two sides of the wake appears also greatly amplified. In particular, the upwind side of the wake ($-0.5 < Y/D < 0$) shows a relatively limited unsteadiness and is dominated by the shear layer between the turbine wake and the outer flow. Conversely, the downwind side of the wake ($0 < Y/D < 0.5$) exhibits large unsteady fluctuations, both in terms of velocity and turbulence intensity, characterized

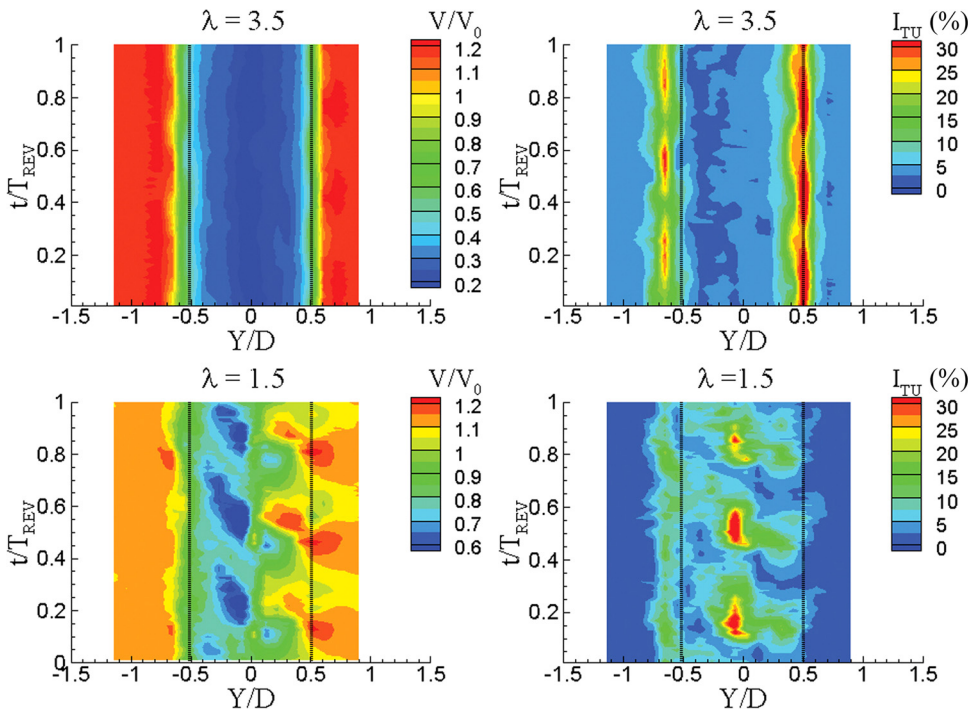

Fig. 17 Space–time wake representation at midspan for $\lambda = 3.5$ (top) and $\lambda = 1.5$ (bottom) in CC configuration

by a deterministic blade-periodic evolution. The space–time turbulence field indicates that the unsteadiness is caused by large-scale, highly turbulent structures that periodically reach the down-stream traverses. The scale (too large for being consistent with the blade wake), the blade-periodic character, and the position of these structures suggest to identify them as separated regions peri-odically detached from the profiles as the blades undergo period excursions under stalled conditions. The onset of dynamic stall is, therefore, responsible for the nonsymmetric shape of the time-mean wake observed at midspan for $\lambda = 1.5$ in Figs. 11(c) and 14(b).

An even larger asymmetry features the wake in the tip region, as shown by the space–time diagrams reported in Fig. 16. Due to the inclined shape of the wake observed in the time-mean plots (see Figs. 11(c) and 14(b)), no wake traces appear on the down-wind side of the wake at the tip section. On the contrary, and dif-ferently with respect to what observed at midspan, the upwind side of the wake now shows a significant periodic unsteadiness; this probably marks the time-evolution of the tip vortex observed in the time-mean flow. The unsteady character of the tip vortex can be explained by resorting to the working principle of VAWTs; as confirmed by the unsteady measurements at midspan, stall is inhibited in the upwind portion of the revolution, resulting in a significant lifting force established on the blades. This leads to a stronger tip vortex on this side of the wake. The periodic oscilla-tion in angle of attack that anyhow occurs during the upwind blade motion affects the generation of the tip vortex, which even-tually appears as a time-dependent structure in the wake down-stream of the turbine.

The time-mean wake properties have been observed to be weakly affected by the wind tunnel confinement; to investigate the effect of turbine blockage on the time-resolved wake features, Fig. 17 reports the space–time diagrams at midspan for the CC configuration in both the highest and the lowest tip-speed ratio considered. These plots, compared with the corresponding ones of Fig. 15, indicate that the confinement does not significantly affect the wake also on a time-resolved basis; as found for OC tests, also in the CC configuration the midspan velocity field is virtually steady for the highest tip-speed ratio, while significant blade-periodic oscillations arise for the lowest tip-speed ratio. The very similar unsteady features observed in this operating condition for OC and CC configurations suggest that the physics of dynamic stall is not significantly affected by the turbine blockage, at least for the low level of loading in which dynamic stall is triggered in this machine.

The turbulence intensity plots also confirm that most of the features observed in unconfined environment are retained in the CC configuration. The only visible difference is a slightly larger blade-periodic unsteadiness for $\lambda = 3.5$ on both the wake sides; this might be due to either a larger fluctuation of angle of attack or a reduced mixing rate between the wake and the outer flow occurring in confined environment; the quantitative impact of this feature is, however, very weak.

The similarity in the velocity and turbulence fields between confined and unconfined configurations represents a relevant finding of the present study; when setting the operating conditions in the CC configuration, the upstream wind velocity was indeed selected considering the blockage correction factor evaluated experimentally (and reported in Fig. 9 of the present paper). The experiments confirm that, by applying a reliable blockage correction procedure, not only the integral quantities but also the flow features are retained when passing from the confined to the unconfined configuration.

Conclusions

In this paper, the results of wide experimental study on a small-scale VAWT have been presented. The experimental campaign, performed in the large-scale wind tunnel of Politecnico di Milano, considered both turbine performance and wake aerodynamic measurements; tests covered a wide range of operative conditions, so to include configurations characterized by dynamic stall, peak efficiency, and very high load. Both open and closed chamber configurations were investigated to quantify experimentally the wind tunnel blockage.

The curves of aerodynamic power and axial thrust coefficient measured in both a confined and unconfined environment have been presented and have been used to compute the experimental blockage factor between closed and open chamber configurations. Results show that that the solid blockage of the rotor and the hull (almost 10%) introduces a non-negligible interference with the wind tunnel walls. The blockage correction factor is found to strongly depend on the operative regime, increasing as the aerody-namic load (and tip-speed ratio) increases. The comparison with well-established blockage models, not satisfactory from both the qualitative and quantitative point of views, indicates the need of specific blockage correction models for VAWTs.

The wake downstream of the turbine was investigated using time-resolved hot wire data in three operating conditions, namely, low load, maximum C_P, and high load for two traverses down-stream of the machine. The velocity fields show that the wake strongly depends on the operating condition, progressively enlarg-ing as the load level increases.

For low aerodynamic loading ($\lambda = 1.5$), a significant asymmetry in the wake shape is observed, both at midspan and at the tip; time-resolved velocity measurements reveal that dynamic stall occurs in the downwind part of the revolution, resulting in a large-scale blade-periodic wake unsteadiness; at the blade tip, the tip vortex dominates the flow field, showing a dramatic asymmetry between the upwind and the downwind portion of the wake as well as large time-dependent fluctuations. As the loading increases, no traces of dynamic stall appear in the downstream flow field; for peak efficiency ($\lambda = 2.5$) and high loading condi-tions ($\lambda = 3.5$), the level of unsteadiness reduces and steady flow in the wake is found; a more symmetric wake shape is also observed.

Wake measurements were also performed in the confined environment; in these tests, the upstream wind speed was set in corresponding conditions with open tunnel experiments, by applying the velocity correction coefficient determined from thrust measurements. A remarkable similarity in the velocity and turbulence fields was found between the confined and the uncon-fined environment, suggesting that the blockage correction pro-cedure here used, only based on integral data, allows to preserve also the detailed flow morphology. This further demonstrates the importance of reliable blockage correlations for the present technology.

Acknowledgment

The authors would like to thank the MIUR (Italian Ministry of Education, University and Research) for funding the research pro-ject, the Company Tozzi-Nord Wind Turbines for rotor design and manufacturing, and the technicians and collaborators of Poli-tecnico di Milano and Università di Trento for their support in performing the measurement campaign.

Nomenclature

A_D = model swept area (m^2)
A_T = closed tunnel area (m^2)
$A_{w,d}$ = downstream wake area (m^2)
$A_{3,exp}$ = experimental wake area (m^2)
$A_{3,model}$ = predicted wake area (m^2)
c = blade chord (m)
C_P = power coefficient
C_{TX} = streamwise trust coefficient
CC = closed chamber configuration
CFRP = carbon fiber reinforced plastic
D = turbine diameter (m)

H = half-blade height (m)
I_{TU} = turbulence intensity (%)
N = number of blades
OC = open chamber configuration
PIV = particle image velocimetry
t = time (s)
T_X = streamwise thrust (N)
T_{rev} = rotor rotation period (s)
V_0 = upstream wind velocity (V_{CC} or V_{OC}) (m/s)
V_0' = corrected upstream wind velocity (m/s)
V_0'/V_0 = blockage correction coefficient
V_{CC} = closed chamber wind speed (m/s)
V_{OC} = open chamber wind speed
$V_{3,dist}$ = downwind disturbed wind velocity (m/s)
VAWT = vertical axis wind turbine

Greek Symbols

$\alpha = A_D/A_T$ = solid blockage ratio
β = Mikkelsen–Sørensen coefficient
ϵ_C = induced velocity at the model position due to collector effect
ϵ_N = induced velocity at model position due to nozzle effect
ϵ_S = induced velocity due to jet expansion
$\lambda = (\omega D/2/V_0)$ = tip-speed ratio
ρ = air density (kg/m^3)
$\sigma = A_{w,d}/A_T$ = downstream wake blockage ratio
Ω = rotor rotational speed (rpm)
ω = rotor angular speed (rad/s)

Coordinate System

X = streamwise axis
X/D = dimensionless streamwise coordinate
Y = transversal axis
Y/D = dimensionless transversal coordinate
Z = vertical axis
Z/H = dimensionless vertical coordinate

References

[1] Sutherland, H. J., Berg Dale, E., and Ashwill, T. D., 2012, "A Retrospective of VAWT Technology," Sandia National Laboratories, Report No. SAND2012-0304.

[2] Bhutta, M. M. A., Hayat, N., Farooq, A. U., Ali, Z., Jamil, S. R., and Hussain, Z., 2012, "Vertical Axis Wind Turbine—A Review of Various Configurations and Design Techniques," Renewable Sustainable Energy Rev., **16**(4), pp. 1926–1939.

[3] IEC (International Electrotechnical Commission) Standard, 2013, *Wind turbines—Part 2: Small Wind Turbines*, IEC, Geneva, Switzerland.

[4] Battisti, L., Zanne, L., Dell'Anna, S., Dossena, V., Persico, G., and Paradiso, G. B., 2011, "Aerodynamic Measurements on a Vertical Axis Wind Turbine in a Large Scale Wind Tunnel," ASME J. Energy Resour. Technol., **133**(3), p. 031201.

[5] Chen, T. Y., and Liou, L. R., 2011, "Blockage Corrections in Wind Tunnel Tests of Small Horizontal Axis Wind Turbines," Elsevier Exp. Therm. Fluid Sci., **35**(3), pp. 565–569.

[6] Ferreira, C. S., van Bussel, G. J. W., et al., 2007, "2D PIV Visualization of Dynamic Stall on a Vertical Axis Wind Turbine," 45th AIAA Aerospace Sciences Meeting 2007, 8-11 January 2007, Reno, NV.

[7] Hofemann, C., Ferreira, C. S., et al., 2008, "3D Stereo PIV Study of Tip Vortex Evolution on a VAWT," Proceedings of the European Wind Energy Conference and Exhibition EWEC, Brussels, European Wind Energy Association (EWEA).

[8] Ferreira, C. S., van Kuik, G., and van Bussel, G. J. W., 2006, "Wind Tunnel Hotwire Measurements, Flow Visualization and Thrust Measurement of a VAWT in Skew," ASME J. Sol. Energy Eng., **128**(4), pp. 487–497.

[9] Ferreira, C. S., van Kuik, G., van Bussel, G. J. W., and Scarano, F., 2009, "Visualization by PIV of Dynamic Stall on a Vertical Axis Wind Turbine," Exp. Fluids, **46**(1), pp. 97–108.

[10] Tescione, G., Ragni, D., He, C., Ferreira, C. S., and van Bussel, G. J. W., 2014, "Near Wake Flow Analysis of a Vertical Axis Wind Turbine by Stereoscopic Particle Image Velocimetry," Renewable Energy, **70**(October), pp. 47–61.

[11] Howell, R., Qin, N., Edwards, J., and Durrani, N., 2010, "Wind Tunnel and Numerical Study of a Small Vertical Axis Wind Turbine," Renewable Energy, **35**(2), pp. 412–422.

[12] Akay, B., Ferreira, C. S., van Bussel, G. J. W., and Tescione, G., 2010, "Experimental and Numerical Investigation of the Effect of Rotor Blockage on Wake Expansion," Proceedings of the 3rd EWEA Conference-Torque 2010: The Science of making Torque from Wind, Heraklion, Crete, Greece, June 28–30, European Wind Energy Association.

[13] Glauert, H., 1933, "Wind Tunnel Interference on Wings, Bodies and Airserews," British A.R.C., R&M No. 1566.

[14] Glauert, H., 1935, "Airplane propellers," *Division L of Aerodynamic Theory*, Vol. 4, W. F. Durand, ed., pp. 169–360, Springer, New York.

[15] Mikkelsen, R., and Sørensen, J. N., 2002, "Tunnel Blockage," Proceedings of the Global Windpower Conference and Modeling of Wind Exhibition.

[16] Sørensen, J. N., Shen, W. Z., and Mikkelsen, R., 2006, "Wall Correction Model for Wind Tunnels With Open Test Section," AIAA J., **44**(8), pp. 1890–1894.

[17] International Organization for Standardization, 2000, "Guide to the Expression of Uncertainty in Measurement (GUM)," UNI-CEI-ENV 13005:2000.

[18] Mercker, E., and Wiedemann, J., 1996, "On the Correction of Interference Effects in Open Jet Wind Tunnels," SAE Paper No. 960671.

[19] Brochier, G., Fraunié, P., Beguiér, C., and Paraschivoiu, I., 1986, "Water Channel Experiments of Dynamic Stall on Darrieus Wind Turbine Blades," J. Propulsion Power, **2**(5), pp. 445–449.